

Attitude estimation from polarimetric cameras

Mojdeh Rastgoo¹, Désire Sidibé¹, Ralph Seulin¹, Cedric Demonceaux¹, Olivier Morel¹

Abstract— In the robotic field, navigation and path planning applications benefit from a wide range of visual systems (e.g. perspective cameras, depth cameras, catadioptric cameras, etc.). In outdoor conditions, these systems capture information in which sky regions cover a major segment of the images acquired. However, sky regions are discarded and are not considered as visual cue in vision applications. In this paper, we propose to estimate attitude of Unmanned Aerial Vehicle (UAV) from sky information using a polarimetric camera. Theoretically, we provide a framework estimating the attitude from the skylight polarized patterns. We showcase this formulation on both simulated and real-word data sets which proved the benefit of using polarimetric sensors along with other visual sensors in robotic applications.

I. INTRODUCTION

Large-field cameras and lenses (e.g. omnidirectional and fisheye cameras) are popular in robotic applications due to their ability to provide large field of view (up to 360°), extending the amount of visual information. It is the main reason for which they have been adopted for a broad range of tasks such as visual odometry [28], navigation [34], simultaneous localization and mapping (SLAM) [15], and tracking [16]. With those systems, sky regions in the images acquired represent a large segment of information which are usually discarded. Here, we show that polarimetric information can be extracted from those regions and used in robotic applications.

Sun position, stars and sky patterns are hold as navigational cues for the past centuries. Indeed, before the discovery of magnetic compass, these natural cues have been the solitary source of navigation used by our ancestors [2, 12]. Similarly, some insects used the skylight polarized pattern created by the scattered sunlight to navigate in their environment [33, 17]. For instance, desert ants (*cataglyphis*), butterflies and dragonflies among others, are able to navigate through their paths, efficiently and robustly by using the polarized pattern of sky, despite their small brains [17, 33, 10].

Acknowledging the nature, numerous studies have been conducted on polarized skylight pattern [18, 4, 35, 32, 3, 1, 30, 20, 22, 31, 19, 10]. These studies are generally reported in the optic field. They focus on estimating the solar azimuth angle by creating a sort of compass. Estimating polarized patterns have been, however, a difficult and complex task. The primary studies report the use of several photodiodes [18, 4, 35, 32, 3], or of multiple cameras [1, 30, 31] or manually rotating filters [20, 22, 19, 10]. As a consequence

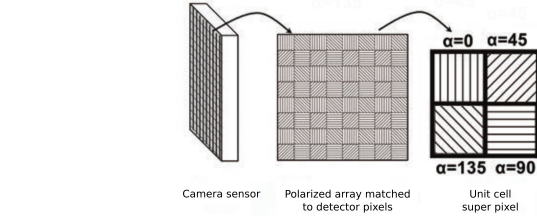


Fig. 1. Structure of DoFP sensors. Using this sensor four linearly polarized image corresponding to the four orientation of the polarized filters is acquired instantly

of those troublesome setups, robotic applications are not benefiting from the advantages of polarized patterns, as attested by the lack of polarized sensors used in Unmanned Aerial Vehicle (UAV). However, the recent introduction of division-of-focal-plane (DoFP) micropolarizer cameras has offered an alternative solution [24, 23, 21]. In such cameras a micropolarizer filter array, composed of a pixelated polarized filters oriented at different angles, is aligned with a detector array. Thus, linear polarization information are simultaneously acquired taking a single image. Here, we use a DoFP coupled with a fisheye lens to exploit the polarized information of sky region to estimate vehicle attitude.

In this paper, Sect. II presents the specificity of the camera used and the adaptation required for our robotic application. The remainder of the paper is organized as follows: Sect. III introduces the concepts of polarization by scattering, Rayleigh model and its relation with attitude estimation. Our formulation to estimate attitude is presented in Sect. IV. Experiments and implementation details are given in Sect. V, and finally discussions and conclusions are drawn in Sect. VI.

II. SETTING THE POLARIMETRIC CAMERA FOR ROBOTICS

As mentioned previously, in this work we use a DoFP polarimetric camera, to be exact *IMPREX Bobcat GEV polarimetric camera*. This camera has the advantage to capture four different linearly polarized measure in one image, due to their micropolarizer and pixelated polarized filter array (see Fig. 1). Therefore each capture image leads to four linearly polarized sub-image I_0 , I_{45} , I_{135} , I_{90} . Using these four measurements, the polarized state of the incident light is calculated in terms of stokes parameters [9], which are used thereafter to calculate polarized parameters such as angle of polarization (AoP) and degree of linear polarization (DoPl) (see Eq. 1).

*This work was not supported by any organization

¹ Université de Bourgogne Franche-Comté, 71200 Le Creusot, France
olivier.morel@u-bourgogne.fr

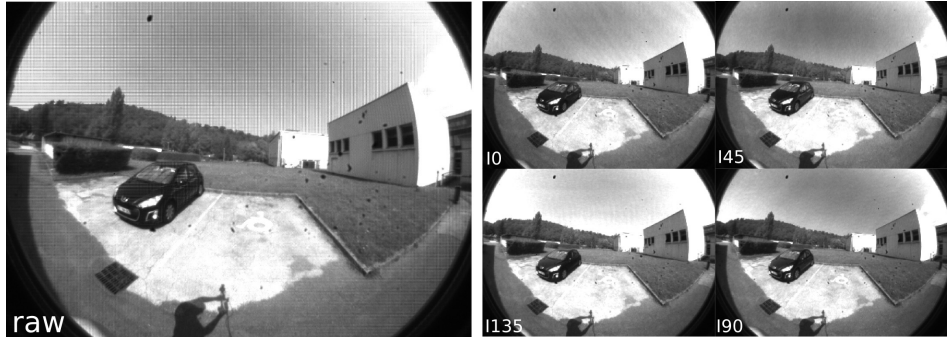


Fig. 2. A raw image captured with fisheye lens, and the extracted four linearly polarized images ($I_0, I_{45}, I_{135}, I_{90}$)

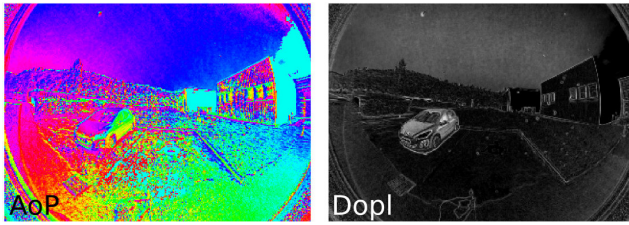


Fig. 3. The AoP, and DoPl images. For visualization purpose, AoP is represented in *hsv* color space.

$$s_0 = (I_0 + I_{45} + I_{135} + I_{90})/4 \quad (1a)$$

$$s_1 = I_0 - I_{90}$$

$$s_2 = I_{45} - I_{135}$$

$$AoP = \alpha = 0.5 \arctan(s_2/s_1) \quad (1b)$$

$$DoPl = \rho_l = \frac{\sqrt{s_2^2 + s_1^2}}{s_0}$$

From the raw images (640×460) captured by the camera, the sub-images can be extracted directly using super-pixel method that leads to four images, half of the size of the raw image, or can be interpolated to the full size [27, 8]. The super-pixel method was used for the results presented in this paper. Being interested in large-field of view, a fisheye lens of 180-degree was used on the camera.

An example of captured raw image, the linearly polarized images and polarized information is shown in Fig. 2 & ??.

The IMPREX *Bobcat GEV* camera operates using eBus SDK-pleora driver and libraries [5]. To be able to use the camera integrated with other sensors, in the robotic field, we have created a ROS package, pleora-polarcam [26]. Initiating from Iralab photonfocus driver [13], pleora-polarcam package is adapted for Imperex polarimetric cameras. Using this package the user can easily roslaunch or rosrun the camera and beside, buffering and saving the raw data, process the stokes and polarized parameters.

III. POLARIZED CUES USED FOR ATTITUDE ESTIMATION

To understand the polarized cues that are used for attitude estimation, three main concepts are covered in this section:

(i) the Rayleigh scattering model and interesting aspects of polarization by scattering, (ii) the polarization parameters in pixel frame and its relation to camera, and (iii) the relationship between the polarized parameters in the pixel frame and other parameters for attitude estimation.

A. Rayleigh scattering model

The unpolarized sunlight passing through our atmosphere gets scattered by different particles within the atmosphere. Beside deviating the direction of propagate wave, this transition also changes the polarization state of the incident light. This transition can be explained using Rayleigh scattering model. Rayleigh scattering describes the scattering of light or any electromagnetic waves by particles much smaller than their transmission wavelength. Accordingly it assumes that scattering particles of the atmosphere are small, homogeneous particles much smaller than the wavelength of the sunlight. Despite its simplification and assumption, this model proved to be sufficient for describing skylight scattering and polarization patterns [25, 11].

The Rayleigh model predicts that the unpolarized sunlight becomes linearly polarized after being scattered by the atmosphere. Based on this model two main outcomes are drawn. On the one hand, the Degree of linear Polarization is directly linked to the scattering angle (γ) according to:

$$\rho_l = \rho_{l_{max}} \frac{1 - \cos^2(\gamma)}{1 + \cos^2(\gamma)} \quad (2)$$

where $\rho_{l_{max}}$ is a constant that should be equal to 1 in theory but in practice the constant is slightly less than 1 due to some atmospheric disturbances[25]. The scattering angle γ is defined by the angle between the observed celestial vector \vec{c} and the sun vector \vec{s} as presented Fig. 4. It can be noticed that the Degree of Polarization is 0 in the sun direction and maximum when the scattering angle is $\pi/2$. [29, 22].

On the other hand, the scattered light is considered to be polarized and orthogonal to the scattering plane. Consequently, the Angle of Polarization is directly related to the orientation of the scattering plane.

B. Polarization by scattering model in pixel frame

As presented Fig. 5, an image is considered as a collection of pixels, and each pixel measures the polarization parameters of the light travelling along a ray associated with that

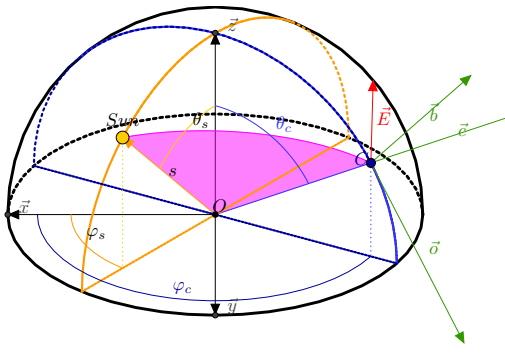


Fig. 4. Skylight polarization by scattering. Scattering plane is highlighted by light shade of red. (θ_s, ϕ_s) and (θ_c, ϕ_c) define the zenith and azimuth angle of sun and celestial point respectively. obc defines the pixel frame, \mathcal{P} , and \vec{E} is the electrical field orthogonal to the scattering plane.

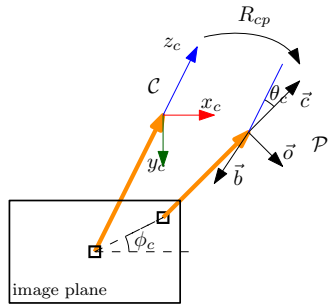


Fig. 5. Rotation between the camera frame C and one pixel frame \mathcal{P} . The light ray associated to the pixels are represented in dark orange. The pixel that corresponds to the center of the image has obviously the same frame as the camera.

pixel. The pixel frame \mathcal{P} is defined accordingly with the ray which coincides with \vec{c} . The camera calibration determines the relationship between pixels and these 3D rays.

Let's consider one pixel of the image with its associated pixel frame \mathcal{P} (obc). Based on Rayleigh scattering the electric field of incident light after scattering is perpendicular to the scattering plane, that is defined by the observer, celestial point and the sun. Accordingly the normalized electric field vector \vec{E} in the world frame is presented as the normalized cross product of \vec{s} and \vec{c} (see Eq. 3).

$$\vec{E} = \frac{\vec{s} \wedge \vec{c}}{\|\vec{s} \wedge \vec{c}\|} \quad (3)$$

The same measure in the pixel frame \mathcal{P} is represented as:

$$E_{obc} = \begin{bmatrix} E_o \\ E_b \\ 0 \end{bmatrix} = \begin{bmatrix} \cos \alpha \\ \sin \alpha \\ 0 \end{bmatrix} \quad (4)$$

where α is the measured AoP associated to the corresponding pixel. Combination of Eq. 3 & 4 and using the scattering angle γ , between \vec{s} and \vec{c} leads to:

$$\begin{cases} (\vec{s} \wedge \vec{c}) \cdot o &= \sin \gamma \cos \alpha \\ (\vec{s} \wedge \vec{c}) \cdot b &= \sin \gamma \sin \alpha \end{cases} \quad (5)$$

applying vector triplet cross product rule on Eq. 5 results.

$$\begin{cases} s \cdot b &= \sin \gamma \cos \alpha \\ s \cdot o &= -\sin \gamma \sin \alpha \end{cases} \quad (6)$$

Using Eq. 2, the scattering angle γ , therefore can be represented as:

$$\cos \gamma = s \cdot c = \pm \sqrt{\frac{1 - \rho'_l}{1 + \rho'_l}} \quad (7)$$

with $\rho'_l = \frac{\rho_l}{\rho_{l_{max}}}$.

Equations 6 & 7 finally leads to a representation of the sun vector in pixel frame \mathcal{P} which express a direct relation between the AoP, the scattering angle and the sun position:

$$\vec{s}_p = \begin{bmatrix} -\sin \gamma \sin \alpha \\ \sin \gamma \cos \alpha \\ \cos \gamma \end{bmatrix} \quad (8)$$

In another word, the sun vector is expressed in the pixel frame as a vector depending only on the polarization parameters AoP and DoPI (which is directly linked to the scattering angle γ).

C. UAV attitude and polarized sky pattern

To derive equations applicable in attitude estimation process, all rotations matrices that describe the frame change must be taken into considerations. The overview of the considered scenario, the frame conventions and rotations for an UAV is shown in Fig. 6. The inertial measurement unit (IMU) frame was added for comparisons purposes.

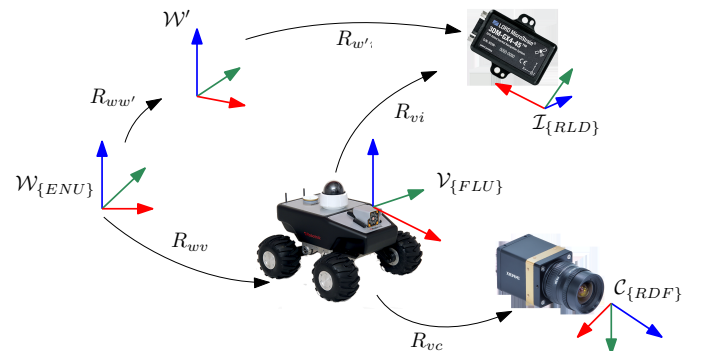


Fig. 6. Frame conventions and rotations for attitude estimation of an UAV

In Fig. 6 the \mathcal{W} , \mathcal{W}' , \mathcal{I} , \mathcal{V} , \mathcal{C} , and \mathcal{P} , present the world frame, global frame of IMU, IMU frame, vehicle frame, camera frame, and pixel frame respectively. Where the rotation from each frame to another is presented with lowercase alphabet. In the shown scenario, a vector v_p in pixel frame is expressed in the world frame, v_w :

$$v_w = R_{wv} \cdot R_{vc} \cdot R_{cp} \cdot v_p \quad (9)$$

where the rotation from the camera to the pixel frame R_{cp} is obtained by camera calibration. The rotation is defined as

the yaw and pitch rotation by the zenith and azimuth angle of the celestial point (θ_c, ϕ_c) as shown in Eq. 10.

$$R_{cp} = \begin{bmatrix} \cos \theta_c \cos \phi_c & -\sin \phi_c & \sin \theta_c \cos \phi_c \\ \cos \theta_c \sin \phi_c & \cos \phi_c & \sin \theta_c \sin \phi_c \\ -\sin \theta_c & 0 & \cos \theta_c \end{bmatrix} \quad (10)$$

$$= R_{z_c}(\phi_c) \cdot R_{y_c}(\theta_c)$$

Previously we presented how to express sun position in pixel frame (see Eq. 8). Indeed this representation is applied to any point from world frame, ergo:

$$s_w = R_{wv} \cdot R_{vc} \cdot R_{cp} \cdot \begin{bmatrix} -\sin \gamma \sin \alpha \\ \sin \gamma \cos \alpha \\ \cos \gamma \end{bmatrix} = R_{wv} \cdot R_{vc} \cdot v$$

$$R^T \cdot s_w = v \quad (11)$$

The above equation shows a direct relationship between the rotation matrix of the vehicle R , the angle of polarization α (that can be measured by the polarimetric camera at one pixel) and the angle of scattering γ for the corresponding pixel. In addition, if ρ_{lmax} is known, the angle of scattering could be directly obtained by inverting equation 7 providing a direct relation between polarization parameters and the rotation of the vehicle.

IV. ATTITUDE ESTIMATION

In this section, a method is first proposed to estimate the scattering angle γ without any assumption regarding the constant ρ_{lmax} which can not be estimated in general. Then two approaches are considered. The first one, called absolute rotation, makes the assumption that the sun position is known or can be deduced from time and the GPS location of the vehicle. The second called relative rotation enables to estimate the relative rotation of the vehicle from the initial position of the vehicle without any additional assumption regarding the sun position.

A. γ estimation

Considering that we are only measuring the angle of polarization α in scattering effects, we have to estimate γ to get the vector v defined in Eq. 11. This equation is valid for all the points in sky region. However with only two celestial points, γ can be estimated as expressed in the following.

$$\begin{cases} R^t \cdot s = R_{cp_1} \cdot \begin{bmatrix} -\sin \gamma_1 \sin \alpha_1 \\ \sin \gamma_1 \cos \alpha_1 \\ \cos \gamma_1 \end{bmatrix} \\ R^t \cdot s = R_{cp_2} \cdot \begin{bmatrix} -\sin \gamma_2 \sin \alpha_2 \\ \sin \gamma_2 \cos \alpha_2 \\ \cos \gamma_2 \end{bmatrix} \end{cases} \quad (12)$$

Using the product of R_{cp} and $R_z(\alpha)$, Eq. 12 is rewritten as:

$$M_1 \cdot \begin{bmatrix} 0 \\ \sin \gamma_1 \\ \cos \gamma_1 \end{bmatrix} = M_2 \cdot \begin{bmatrix} 0 \\ \sin \gamma_2 \\ \cos \gamma_2 \end{bmatrix} \quad (13)$$

By defining the matrix M such that $M = M_2^T \cdot M_1$, γ_1 and γ_2 are found as:

$$\begin{cases} \gamma_1 = -\arctan \frac{M_{02}}{M_{01}} \\ \gamma_2 = -\arctan \frac{M_{20}}{M_{10}} \end{cases} \quad (14)$$

The AoP is 2π modulus, while the γ found in Eq. 14 is π modulus, this leads to two possible solutions for vector v , (α_1, γ_1) and $(\alpha_1 + \pi, -\gamma_1)$.

B. Absolute rotation

In order to estimate the absolute rotation and attitude of the UAV, it is assumed that: (i) the sun position is known, (ii) using the AoP measures of the sky (2 points), the vector v is estimated, (iii) either using the AoP from horizontally reflected areas (i.e. water) a second vectors w is estimated or the vertical in the pixel frame is known. In this study we assumed that the vertical in the pixel frame is known, however having any horizontal surface, the second vector can be estimated.

The aforementioned assumptions leads to the following expression, where z is the vertical in world frame $([0, 0, 1])$ and t is the time instance.

$$\begin{cases} [s, z, s \wedge z] = R(t) \cdot [v(t), w(t), v(t) \wedge w(t)] \\ = R_{wv}(t) \cdot R_{vc} \cdot [v(t), w(t), v(t) \wedge w(t)] \end{cases} \quad (15)$$

Solving Eq. 15 enables to get $R_{wv}(t)$. However due to γ ambiguities, there exist two solutions for v and therefore for R_{wv} . To constraint the solutions, at each time stamp, a closest solution compare to the previous time stamp is selected.

C. Relative rotation

The relative rotation is estimated between two different time stamps (t_1, t_2). Therefore Eq. 15 becomes (For simplicity in the rest, $v(t_1)$ and $v(t_2)$ are referred as v_1 and v_2):

$$\begin{cases} [s, z, s \wedge z] = R_{wv1} \cdot R_{vc} \cdot [v_1, w_1, v_1 \wedge w_1] \\ [s, z, s \wedge z] = R_{wv2} \cdot R_{vc} \cdot [v_2, w_2, v_2 \wedge w_2] \end{cases} \quad (16)$$

which leads to:

$$R_{wv2} = R_{wv1} \cdot R_{vc} \cdot [v_1, w_1, v_1 \wedge w_1] \cdot [v_2, w_2, v_2 \wedge w_2]^{-1} \cdot R_{vc}^T. \quad (17)$$

Using the above equation, the relative rotation $R_{v_1 v_2}$ is equal to:

$$R_{v_1 v_2} = R_{vc} \cdot [v_1, w_1, v_1 \wedge w_1] \cdot [v_2, w_2, v_2 \wedge w_2]^{-1} \cdot R_{vc}^T \quad (18)$$

The basic theory of attitude estimation based on polarization by scattering was explained in this section emphasizing that in both approaches, only two points from the pattern of the sky are required to solve the scattering angle γ . As described in the following section, an algorithm to robustify the results is implemented by considering more points.



Fig. 7. The setup used for acquiring presented datasets in this paper

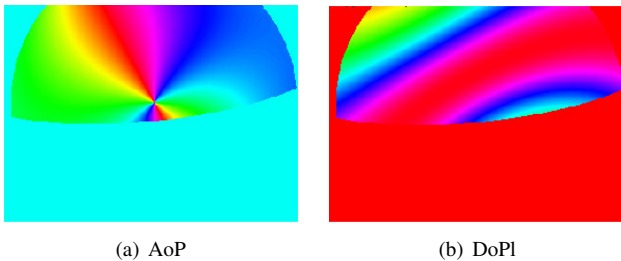


Fig. 8. Synthetically created AoP and DoPI images of sky region for yaw, pitch and roll angle of 1.8, -0.2 and 0.1, respectively.

V. EXPERIMENTS AND RESULTS

This section presents our setup, the designed experiments and the obtained results. The setup used in our experiment is based on fig. 6. However instead of using a UAV, a camera was manually moved (see Fig. 7). To be able to use the IMU recordings as ground-truth (GT), this device was calibrated with the camera using kalibr toolbox [7, 6]. The polarimetric camera with fisheye lens was also calibrated according to [14].

Using the above setup two data sets of synthetic and real images were created and the results obtained are presented in Exp. V-A and Exp. V-B, respectively.

A. Experiment 1

The synthetic data containing AoP and DoPI images of sky regions were created using the IMU recordings obtained during real acquisition. Figure 8 shows an example of this dataset at optimal conditions.

Applying our framework on ideal synthetic data, perfect results were obtained for absolute and relative rotations, while γ was estimated using only two random points from sky region (see Fig. 9). The synthetic dataset created based on IMU recordings, has rotation of roll, pitch and yaw, respectively. This dataset has 856 samples, however for simplicity, it has been down sampled by sampling rate of 30 samples.

Although using our proposed framework we were able to achieve perfect results on ideal synthetic data, in reality it is rare to obtain the perfect skylight polarization pattern. Variety of causes clutter the desired skylight pattern, main one being pollution. To account for such cases, a second test was performed while significant level of noise was added to the created synthetic data. Figure 10 shows an example of synthetic data with %10 noise.

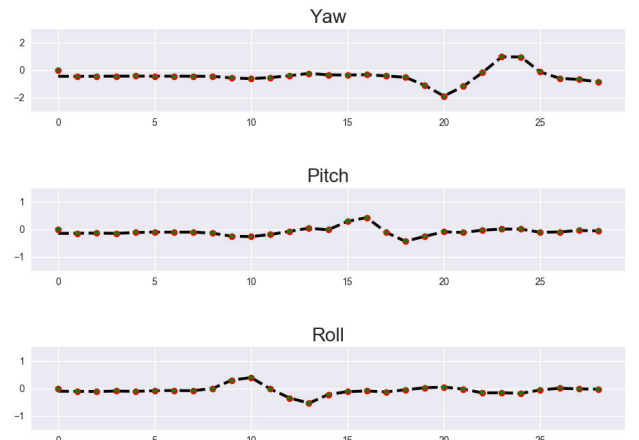


Fig. 9. Absolute and relative rotation obtained from synthetic data in optimal conditions. The black line represents the GT, the dots and the stars represent the absolute and relative predicted rotations, respectively.

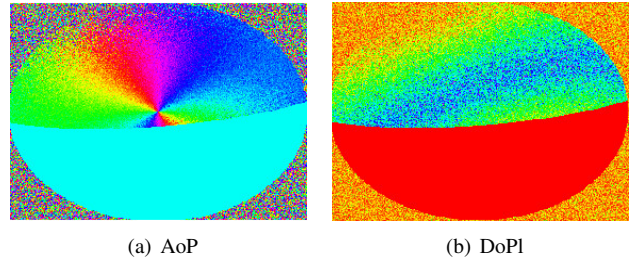


Fig. 10. Synthetically created AoP and DoPI images of sky region with noise level of 0.1. With yaw, pitch and roll angle of 1.8, -0.2 and 0.1, respectively.

Performing the same 2-random-point algorithm as before on noisy dataset leads to the results illustrated in Fig. 11(a). As expected the performance decline, simply due to the noise.

To solve this problem, two ransac models were defined for the absolute and relative rotation, respectively. In the proposed ransac model for absolute rotation, since the sun position is assumed to be known the ransac model optimizes the full rotation of each frame in comparison to the origin considering the difference between the predicted and real sun positions.

The relative model, however, there is no information about the original position, or sun position, and the algorithm only depends on the polarized vector, $v = R_{cp} * v_p$ between two different frames. Therefore using the ransac model, the optimal vector representing each frame is obtained.

Running our ransac models on the noisy datasets, with error threshold of 0.07, 10 random points (2 points for defining the model and the rest as test), and 2000 iterations the following results are obtained:

The quantitative results in terms of mean difference (μ) and standard deviation (σ) between the predicted rotations and GT are tabulated in Table. I.

As illustrated in the obtained results, using the ransac model the outliers are ignored and satisfactory results are

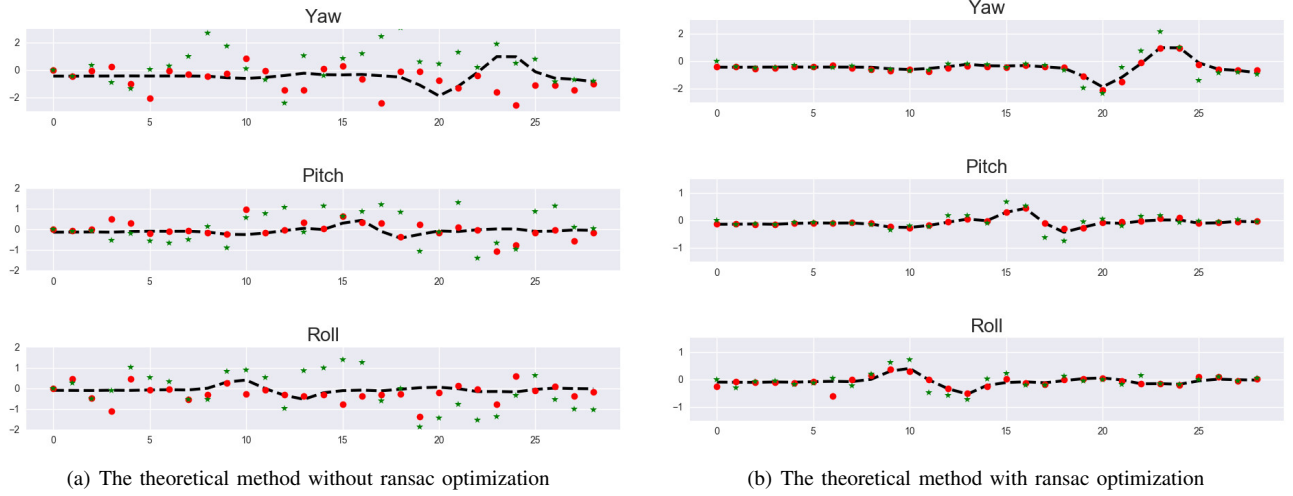


Fig. 11. Absolute and relative rotation obtained from noisy synthetic data without and with ransac optimization. The black line represents the GT, the dots and the stars represent the absolute and relative predicted rotations, respectively.

TABLE I
MEAN DIFFERENCE AND STANDARD DEVIATION COMPARISON BETWEEN PREDICTED RESULTS AND GT IN RADIAN.

	Yaw		Pitch		Roll	
	μ	$\pm\sigma$	μ	$\pm\sigma$	μ	$\pm\sigma$
Absolute	0.087	0.078	0.020	0.029	0.068	0.100
Relative	0.275	0.35	0.113	0.123	0.148	0.111

TABLE II
MEAN DIFFERENCE AND STANDARD DEVIATION COMPARISON BETWEEN PREDICTED RESULTS AND GT IN RADIAN ON REAL DATA.

	Yaw		Pitch		Roll	
	μ	$\pm\sigma$	μ	$\pm\sigma$	μ	$\pm\sigma$
Absolute	0.23	0.22	0.27	0.18	0.18	0.19
Relative	0.37	0.40	0.20	0.18	0.20	0.18

achieved.

B. Experiment 2

This section presents the results obtained using real data. Same as previous experiment the IMU results were used to create the GT for vehicle pose in the world frame. The original data set contains 593 recordings. However for simplicity it was down sampled with sampling rate of 20 frames. Running ransac optimization with the same criteria as previous experiment the following results are obtained (see Fig. 12 & Table. II).

VI. DISCUSSION AND CONCLUSION

This paper presents the results of our attitude estimation using polarimetric camera and skylight polarized pattern. The proposed algorithm was tested using real and synthetic data. In order to cope with the undesired artifacts and outliers in the measurements, we integrated a ransac model in our framework. Promising results were achieved after using

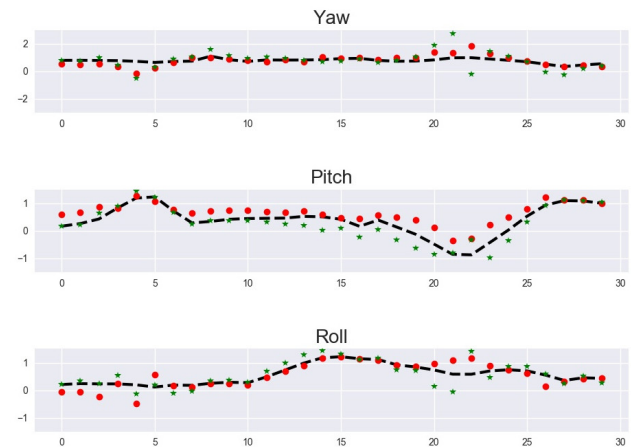


Fig. 12. Absolute and relative rotation obtained from real data. The black line represents the GT, the dots and the stars represent the absolute and relative predicted rotations, respectively.

ransac optimization. However, certainly, there is room for improvements for instance minimizing the accumulated error of prediction using a filter. Nevertheless, in this paper we presented the potential and capacity of a polarimetric camera and polarized information to be integrated in the robotic field.

As a future works, as presented in [10], we would like to integrate the use of DoPI for attitude estimation and assess the performance of the polarimetric camera in combination of traditional sensors.

REFERENCES

- [1] J. R. Ashkanazy and J. Humbert, "Bio-inspired absolute heading sensing based on atmospheric scattering," in *AIAA Guidance, Navigation, and Control Conference*, 2015, p. 0095.
- [2] A. Barta, V. B. Meyer-Rochow, and G. Horváth, "Psychophysical study of the visual sun location in pictures of cloudy and twilight skies inspired by viking navigation," *JOSA A*, vol. 22, no. 6, pp. 1023–1034, 2005.
- [3] J. Chahl and A. Mizutani, "Integration and flight test of a biomimetic heading sensor," in *Proc. SPIE*, vol. 8686, 2013, p. 86860E.

- [4] J. Chu, H. Wang, W. Chen, and R. Li, "Application of a novel polarization sensor to mobile robot navigation," in *International Conference on Mechatronics and Automation. ICMA 2009.* IEEE, 2009, pp. 3763–3768.
- [5] eBus SDK, "eBUS SDK | Pleora Technologies Inc," <http://www.pleora.com/our-products/ebus-sdk>, 2018.
- [6] P. Furgale, T. D. Barfoot, and G. Sibley, "Continuous-time batch estimation using temporal basis functions," in *Robotics and Automation (ICRA), 2012 IEEE International Conference on.* IEEE, 2012, pp. 2088–2095.
- [7] P. Furgale, J. Rehder, and R. Siegwart, "Unified temporal and spatial calibration for multi-sensor systems," in *Intelligent Robots and Systems (IROS), 2013 IEEE/RSJ International Conference on.* IEEE, 2013, pp. 1280–1286.
- [8] S. Gao and V. Gruev, "Bilinear and bicubic interpolation methods for division of focal plane polarimeters," *Optics express*, vol. 19, no. 27, pp. 26 161–26 173, 2011.
- [9] D. H. Goldstein, *Polarized light.* CRC press, 2017.
- [10] M. Hamaoui, "Polarized skylight navigation," *Applied Optics*, vol. 56, no. 3, pp. B37–B46, 2017.
- [11] G. Horvath, A. Barta, J. Gal, B. Suhai, and O. Haiman, "Ground-based full-sky imaging polarimetry of rapidly changing skies and its use for polarimetric cloud detection," *Applied optics*, no. 3, pp. 543–559, 2002.
- [12] G. Horváth, A. Barta, I. Pomozi, B. Suhai, R. Hegedüs, S. Åkesson, B. Meyer-Rochow, and R. Wehner, "On the trail of vikings with polarized skylight: experimental study of the atmospheric optical prerequisites allowing polarimetric navigation by viking seafarers," *Philosophical Transactions of the Royal Society of London B: Biological Sciences*, vol. 366, no. 1565, pp. 772–782, 2011.
- [13] Iralab, "ROS device driver for PhotonFocus cameras based on Pleoras eBUS Software Development Kit (SDK)," https://github.com/iralabdisco/ira_photonfocus_driver, 2018.
- [14] J. Kannala and S. S. Brandt, "A generic camera model and calibration method for conventional, wide-angle, and fish-eye lenses," *IEEE transactions on pattern analysis and machine intelligence*, vol. 28, no. 8, pp. 1335–1340, 2006.
- [15] J.-H. Kim and M. J. Chung, "Slam with omni-directional stereo vision sensor," in *International Conference on Intelligent Robots and Systems, 2003*, vol. 1. IEEE, 2003, pp. 442–447.
- [16] M. Kobilarov, G. Sukhatme, J. Hyams, and P. Batavia, "People tracking and following with mobile robot using an omnidirectional camera and a laser," in *IEEE International Conference on Robotics and Automation, ICRA.* IEEE, 2006, pp. 557–562.
- [17] T. Labhart and E. P. Meyer, "Neural mechanisms in insect navigation: polarization compass and odometer," *Current opinion in neurobiology*, vol. 12, no. 6, pp. 707–714, 2002.
- [18] D. Lambrinos, R. Müller, T. Labhart, R. Pfeifer, and R. Wehner, "A mobile robot employing insect strategies for navigation," *Robotics and Autonomous Systems*, vol. 30, no. 12, pp. 39 – 64, 2000. [Online]. Available: <http://www.sciencedirect.com/science/article/pii/S0921889099000640>
- [19] H. Lu, K. Zhao, Z. You, and K. Huang, "Angle algorithm based on hough transform for imaging polarization navigation sensor," *Optics express*, vol. 23, no. 6, pp. 7248–7262, 2015.
- [20] T. Ma, X. Hu, L. Zhang, J. Lian, X. He, Y. Wang, and Z. Xian, "An evaluation of skylight polarization patterns for navigation," *Sensors*, vol. 15, no. 3, pp. 5895–5913, 2015.
- [21] J. Millerd, N. Brock, J. Hayes, M. North-Morris, B. Kimbrough, and J. Wyant, "Pixelated phase-mask dynamic interferometers," *Fringe 2005*, pp. 640–647, 2006.
- [22] D. Miyazaki, M. Ammar, R. Kawakami, and K. Ikeuchi, "Estimating sunlight polarization using fish-eye lens," in *IPSJ Transactions on Computer Vision and Applications*, vol. 1, 2009, pp. 288–300.
- [23] G. P. Nordin, J. T. Meier, P. C. Deguzman, and M. W. Jones, "Diffractive optical element for stokes vector measurement with a focal plane array," in *Proc. SPIE*, vol. 3754, 1999, pp. 169–177.
- [24] ——, "Micropolarizer array for infrared imaging polarimetry," *JOSA A*, vol. 16, no. 5, pp. 1168–1174, 1999.
- [25] I. Pomozi, G. Horvath, and R. Wehner, "How the clear-sky angle of polarization pattern continues underneath clouds: full-sky measurements and implications for animal orientation," *The Journal of Experimental Biology*, vol. 204, pp. 2933–2942, 2001.
- [26] M. Rastgoo, "ROS device driver for Imperex polarimetric cameras based on Pleoras eBUS Software Development Kit (SDK)," <https://github.com/I2Cvb/pleora-polarcam>, 2018.
- [27] B. M. Ratliff, C. F. LaCasse, and J. S. Tyo, "Interpolation strategies for reducing ifov artifacts in microgrid polarimeter imagery," *Opt. Express*, vol. 17, no. 11, pp. 9112–9125, May 2009. [Online]. Available: <http://www.opticsexpress.org/abstract.cfm?URI=oe-17-11-9112>
- [28] D. Scaramuzza and R. Siegwart, "Appearance-guided monocular omnidirectional visual odometry for outdoor ground vehicles," *IEEE transactions on robotics*, vol. 24, no. 5, pp. 1015–1026, 2008.
- [29] G. S. Smith, "The polarization of skylight: An example from nature," *American Journal of Physics*, vol. 75, no. 1, pp. 25–35, 2007.
- [30] W. Stürzl and N. Carey, "A fisheye camera system for polarisation detection on uavs," in *European Conference on Computer Vision.* Springer, 2012, pp. 431–440.
- [31] D. Wang, H. Liang, H. Zhu, and S. Zhang, "A bionic camera-based polarization navigation sensor," *Sensors*, vol. 14, no. 7, pp. 13 006–13 023, 2014.
- [32] Y. Wang, J. Chu, R. Zhang, L. Wang, and Z. Wang, "A novel autonomous real-time position method based on polarized light and geomagnetic field," *Scientific reports*, vol. 5, 2015.
- [33] R. Wehner, "Desert ant navigation: how miniature brains solve complex tasks," *J Comp Physiol A*, vol. 189, pp. 579–588, 2003.
- [34] N. Winters, J. Gaspar, G. Lacey, and J. Santos-Victor, "Omnidirectional vision for robot navigation," in *IEEE Workshop on Omnidirectional Vision.* IEEE, 2000, pp. 21–28.
- [35] K. Zhao, J. Chu, T. Wang, and Q. Zhang, "A novel angle algorithm of polarization sensor for navigation," *IEEE Transactions on Instrumentation and Measurement*, vol. 58, no. 8, pp. 2791–2796, 2009.